Exp Fluids (2009) 46:1021–1036
DOI 10.1007/s00348-008-0608-z

RESEARCH ARTICLE

A synthetic Schlieren method for the measurement of the topography of a liquid interface

Frédéric Moisy · Marc Rabaud · Kévin Salsac

Received: 10 June 2008 / Accepted: 19 December 2008 / Published online: 13 January 2009

Abstract An optical method for the measurement of the instantaneous topography of the interface between two transparent fluids, named free-surface synthetic Schlieren (FS-SS), is characterised. This method is based on the analysis of the refracted image of a random dot pattern visualized through the interface. The apparent displacement field between the refracted image and a reference image obtained when the surface is flat is determined using a digital image correlation (DIC) algorithm. A numerical integration of this displacement field, based on a least square inversion of the gradient operator, is used for the reconstruction of the instantaneous surface height, allowing for an excellent spatial resolution with a low computational cost. The main limitation of the method, namely the ray crossing (caustics) due to strong curvature and/or large surface-pattern distance, is discussed. Validation experiments using a transparent solid model with a wavy surface or plane waves at a water–air interface are presented, and some additional time-resolved measurements of circular waves generated by a water drop impact are discussed.

F. Moisy (✉) · M. Rabaud · K. Salsac
Fluides, Automatique et Systèmes Thermiques (FAST),
University of Paris-Sud, Bâtiment 502, Campus Universitaire,
91405 Orsay, France
e-mail: moisy@fast.u-psud.fr

F. Moisy · M. Rabaud · K. Salsac
Fluides, Automatique et Systèmes Thermiques (FAST),
University Pierre et Marie Curie, Bâtiment 502,
Campus Universitaire, 91405 Orsay, France

F. Moisy · M. Rabaud · K. Salsac
Fluides, Automatique et Systèmes Thermiques (FAST), CNRS,
Bâtiment 502, Campus Universitaire, 91405 Orsay, France

1 Introduction

1.1 Review of optical methods measuring surface slopes

The measurement of the deformation of a liquid surface is of fundamental and practical interest in numerous research fields, from small scales (e.g. painting or coating industry) to large scales (e.g. wind waves, ship wakes). Optical methods, being non-intrusive and able to provide an instantaneous two-dimensional measurement, are of much practical interest. Among those methods, the measurement of the surface slope based on light reflection or refraction are the most promising. Those methods have been widely used for one-point measurements of one or two components of the surface slope using laser beam refraction (Tober et al. 1973; Lange et al. 1982; Liu et al. 1993), with possible extension to line measurement using a fast scanning technique (Savalsberg et al. 2006).

Extensions of this approach for two-dimensional fields, pioneered by Cox (1958) for only one slope component, are based on the use of collimated light beam encoded with a linearly increasing intensity, so that a one-to-one mapping between light intensity and slope can be obtained. The main advantage of using collimated light is that the measured gradient is insensitive to the surface height. Zhang et al. have extended the method to the measurements of the two components of the surface gradient, using a system of color-encoded collimated beams, generated by a suitably colored screen and a large lens, operating either in refraction or reflection on the free surface (Zhang and Cox 1994; Zhang et al. 1996). A calibration of the color-slope mapping is required, and can be performed using a glass sphere. From those measurements, the surface elevation could be obtained by integrating the gradient components

in the Fourier domain (Zhang 1996). This method has been succesfully used for the investigation of surface deformations induced by vortices in a shear layer flow (Dabiri and Gharib 2001).

Roesgen et al. (1998) introduced a new approach, also based on collimated light, using an array of microlenses of 200 μm in diameter placed above the free surface. The surface deformation leads to a displacement of the light spots in the focal plane of the microlens array that could be measured using a digital image correlation (DIC) algorithm. The surface height reconstruction was obtained by these authors by a least-square inversion of the linear system built from a finite-difference scheme expressed on the hexagonal lattice of the microlens array. Here again, the size of the microlens array, usually 2–3 cm, limits the size of the imaged area, restricting this approach to small fields.

Using scattered light instead of collimated light allows for simplification of the optical setup, since no collimating lens or mirror is needed, but the resulting measurement is a combination of the surface slope and height. Keller and Gotwols (1983), and later Jähne and Riemer (1990), used a light source of varying intensity along one direction, imaged through the free surface. This approach has been recently combined with a direct measurement of the surface height based on light absorbtion (Jähne et al. 2005).

Another image-encoding approach, first discussed by Kurata et al. (1990), relies on the use of scattered light emitted from a structered pattern, such as a grating or a set of random dots, imaged through the interface. Here the displacement field is obtained by comparing the refracted images of the pattern obtained with flat and deformed surfaces. A similar approach has been used for the measurement of the contact angle of a drop on a solid substrate (Andrieu et al. 1995).

Although originally introduced for surface slope measurements, the approach of Kurata et al. (1990) has been extensively applied to measurements in fluids with density variations, in the so-called "synthetic Schlieren" (SS) (Sutherland et al. 1999; Dalziel et al. 2000) and "Background-Oriented Schlieren" (BOS) methods (Meier 2002). The name "synthetic Schlieren" has been more widely used for stratification-induced density variations in the geophysical fluid dynamics community, whereas the name "Background-Oriented Schlieren" has been mainly used for compressible fluids in the aerodynamics community. In all cases, the displacement field between a reference image and a refracted image originates from the continuous variation of the optical index induced by the density variations, and is measured using a DIC algorithm. However, the displacement at one point being the result of the index variation integrated along a light ray, the refraction index field cannot be inferred in general from those measurements. On the other hand, in the case of a free surface, the step-like variation of the refraction index makes possible a complete reconstruction of the surface height, as noted by Dalziel et al. (2000). Elwell (2004) successfully used this idea to obtain quantitative measurements of the surface deformation induced by vortices in a shallow water flow, using a cumulative sum scheme of the measured gradient components for the surface height reconstruction.

1.2 Outline and scope of the paper

This paper presents a detailed characterisation of the method originally introduced by Kurata et al. (1990) and quantitatively developed by Elwell (2004). We propose the name free-surface synthetic Schlieren (FS-SS) for this method, as it relies on the same physical principle as the now standard synthetic Schlieren method for density-varying fluids. This methods allows for an accurate and low-cost measurement of the instantaneous topography of the interface between two transparent fluids. We show that a precision of 1 μm for a 10-cm field can be readily achieved, making this method attractive for investigation of small-scale waves dynamics or coating phenomena.

The FS-SS method consists in two steps:

1. measurement of the surface gradient from the displacement field of the refracted image of a random pattern using a DIC algorithm;
2. reconstruction of the surface height using a least-square integration of the surface gradient.

Compared to the methods based on collimated light, which require an elaborate optical setup and a delicate calibration scheme, the present method, like the standard synthetic Schlieren method, is simply based on a black-and-white imaging system with simple optics. As a consequence it may be easily reproduced for a large range of applications using standard laboratory equipment. The drawback of this simplified setup is that, since no collimating optics is used, oblique light rays have to be considered, yielding to a more delicate analysis of the ray geometry in the general case. It is shown however that, to first order in paraxial angles, in surface slopes, and in relative deformations, the surface gradient is simply proportionnal to the displacement field.

The computation of the displacement field from the refracted images of the flat and deformed interface is based on a standard DIC algorithm. Due to its wide use in solid and fluid mechanics, DIC (or other pattern matching technics, such as optical flow, Barron et al. 1994) have received considerable interest in recent years, and several commercial and open-source packages are now available. DIC is mainly used in solid mechanics for the measurement

of the strain field at the surface of a solid (Périe et al. 2002; Hild and Roux 2006). In fluid mechanics, apart from synthetic Schlieren applications, DIC algorithms are mostly used in particle image velocimetry (PIV) applications, where the velocity field is given by the displacement field of tracer particles per unit of sampling time (Adrian 1991; Raffel et al. 1998).

The second step of the method, the integration of the gradient field, is based on a least-square inversion of the gradient operator. This procedure, first used by Roesgen et al. (1998) for an hexagonal lattice, is formulated here for a Cartesian lattice. It relies therefore on a simpler numerical scheme, here again available from standard linear algebra packages.

The paper is organized as follows. The relation between the surface gradient and the displacement field is derived in Sect. 2. The experimental set-up and the numerical methods for the measurement of the displacement field and for the reconstruction of the surface height are presented in Sect. 3. Two validation experiments are described in Sect. 4: one using the deflection of a laser beam to validate the displacement field measurement, and one using a transparent solid model to validate the surface height reconstruction. Section 5 discusses the maximum acceptable distorsion for a reliable reconstruction of the surface height. Additional time-resolved experiments of circular waves generated by the impact of a water drop in water are presented in Sect. 6. Finally, Sect. 7 discusses some possible applications of the method.

2 Relation between the surface gradient and the displacement field

2.1 Optical configurations and approximations

We want to determine the optical displacement field $\delta\mathbf{r}(x, y)$ induced by the refraction of the light scattered from a pattern located at $z = 0$ through the interface $z = h(x, y)$. At each object point M of the pattern, we need to determine the virtual objects M' and M'' corresponding to the flat and deformed interface, respectively, and to relate the displacement $\mathbf{M'M''} = \delta\mathbf{r}$ with the surface gradient ∇h at the same point.

The surface is assumed to be smooth enough, so that the light rays reaching the camera cross the surface only once. The pattern may be located either above or below the surface. The refraction indices of the fluids on the camera side and on the pattern side are noted n and n', respectively. This generic formulation encompasses the two following configurations:

Configuration 1 Camera above and pattern below the surface (the most common situation). A limitation of this configuration is that the surface-pattern distance has to be equal or larger than the liquid depth, which may cause ray crossings and caustics for large surface curvature or large depth (discussed in Sect. 2.5).

Configuration 2 Camera below and pattern above the surface (assuming the container has a transparent bottom). In this case, the surface-pattern distance is arbitrary, and may be increased for better resolution, or set as close as possible to the surface to avoid ray crossings when strong curvature of the surface are present.

Configuration 1 is illustrated in Fig. 1 when the interface is flat, and is used as a reference for the derivation of the relation between $h(x, y)$ and $\delta\mathbf{r}(x, y)$. In this configuration,

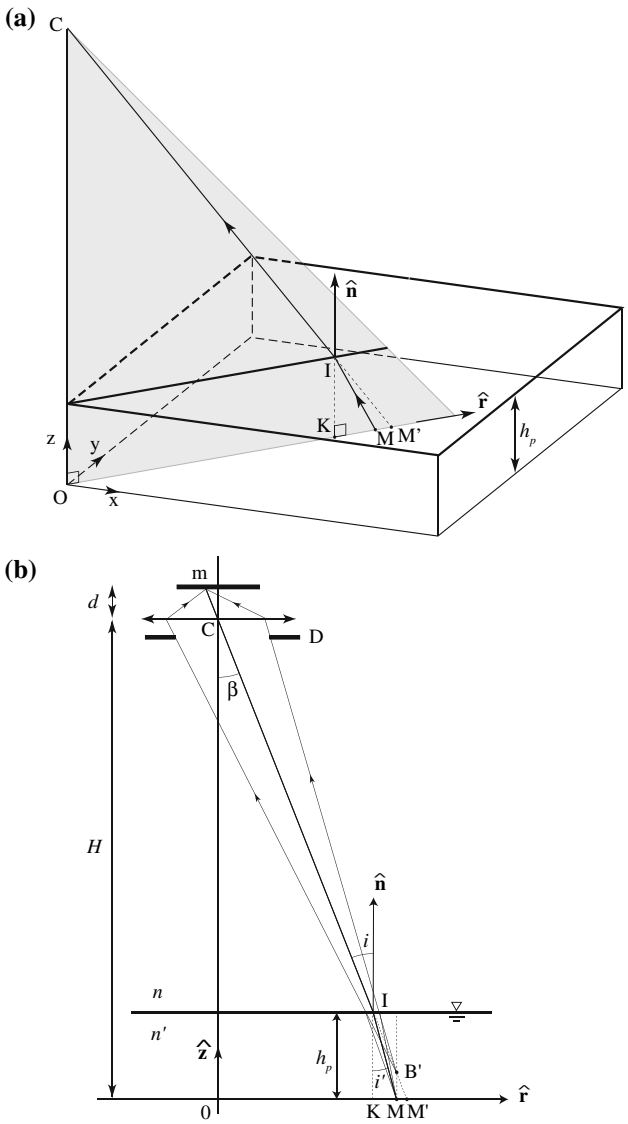

Fig. 1 **a** Three-dimensional ray geometry for a horizontal interface (reference case). **b** Two-dimensional view of the vertical incidence plane COM. A ray coming from a point M located on the pattern appears to come from the virtual object B'. In the pattern plane, it appears to come from the point M'

$n' > n$, so that wave crests and troughs will act as magnifying (convex) and reducing (concave) lenses, respectively. We will use a cartesian frame with the vertical optical axis z crossing the origin O and the camera C, the plane $z = 0$ corresponding to the pattern plane. We note D the diaphragm diameter of the camera, and β the paraxial angle. For the sake of simplicity, the pattern-surface distance h_p is chosen equal to the liquid depth h_0, but optical corrections for additional intermediate layers between the pattern and the surface can be easily included.

In the following, three approximations are considered, based on the three small parameters: the paraxial angle β, the surface slope γ and the relative surface deformation.

1. *Paraxial approximation* The pattern-camera distance H is much larger than the field size L, yielding a maximum paraxial angle $\beta_{max} \simeq L/(\sqrt{2}H) \ll 1$.
2. *Weak slope approximation* The angle γ between the unit vector normal to the interface $\hat{\mathbf{n}}$ and the vertical vector $\hat{\mathbf{z}}$ is small. As a consequence, the surface slope θ measured in the incidence plane is also small.
3. *Weak amplitude approximation* Denoting $h(x, y) = h_p + \eta(x, y)$ the surface height, the amplitude $|\eta|$ is small compared to the mean height h_p.

In the derivation of the relation between ∇h and $\delta\mathbf{r}$, linearisation with respect to those three parameters is performed.

2.2 Refracted image through a horizontal interface

We first consider the refracted image of the pattern at $z = 0$ through a flat interface at $z = h_p$ (Fig. 1). For each point M, located in $(x_M, y_M, 0)$, a vertical incidence plane COM can be defined, crossing the pattern plane along the radial unit vector $\hat{\mathbf{r}} = \mathbf{OM}/|\mathbf{OM}|$. The image of M is m in the image plane (camera sensor), and the corresponding virtual object B' is located above the pattern, in $(x_M, y_M, \alpha h_p)$ with

$$\alpha = 1 - n/n'. \tag{1}$$

In practice, the focus is made on this vertically shifted focal plane at $z = \alpha h_p$. For convenience, since rays reaching the image plane in m appear to come from a point M' in the pattern plane, in the following, the apparent displacements are simply given in the plane $z = 0$.

The displacement from M to M' is outward, in the radial direction, and is given by

$$\mathbf{MM'} = h_p(\tan i - \tan i')\hat{\mathbf{r}}, \tag{2}$$

where the incidence and refracted angles are related by the Snell-Descarte law, $n \sin i = n' \sin i'$. For the flat interface, the incidence angle i is simply equal to the paraxial angle β. Within the paraxial approximation and using Eq. 1, Eq. 2 simplifies to:

$$\mathbf{MM'} = \alpha h_p i\hat{\mathbf{r}}. \tag{3}$$

From the image of the pattern seen through the flat interface, we can determine the location of any point M from the position of its image M' given h_p, H and the location of the optical center O.

2.3 Refracted image through a deformed interface

We consider now the refracted image of the pattern through an arbitrary deformed interface, and we want to determine the new virtual object M'' associated to the given object point M (Fig. 2). This problem is more delicate, since now the incidence plane is not vertical (except for axisymmetric deformations), and does not contain the optical axis z. For a given point M, the incidence plane is defined as the plane containing M, the camera C, and the unit vector $\hat{\mathbf{n}}$ measured at the point I where the light ray MIC intercepts the interface, with

$$\hat{\mathbf{n}} = \frac{\hat{\mathbf{z}} - \nabla h}{\sqrt{1 + |\nabla h|^2}}. \tag{4}$$

Assuming weak slopes, $|\nabla h|^2 \ll 1$, Eq. 4 simply gives:

$$\nabla h = \hat{\mathbf{z}} - \hat{\mathbf{n}}. \tag{5}$$

The displacement $\mathbf{MM''}$ takes place along the direction $\mathbf{s}$ (see the top view in Fig. 3), defined as the intersection of the incidence plane and the horizontal plane $z = 0$, yielding

$$\mathbf{s} = \mathbf{OM}/H - \nabla h.$$

The incident plane CAM, where A is the projection of the origin O on the line MM'', is shown in Fig. 2b. For a camera far above the surface $(H \gg L)$, the plane CAM tends to be vertical and $\mathbf{s}$ becomes aligned with the surface gradient (except for very weak slopes $|\nabla h| \ll |\mathbf{OM}|/H$, for which $\mathbf{s}$ remains essentially radial).

Since $\hat{\mathbf{n}}$, $\mathbf{CM''}$ and $\hat{\mathbf{s}} = \mathbf{MM''}/|\mathbf{MM''}|$ are contained in the incident plane CAM, $\hat{\mathbf{n}}$ can be written as

$$\hat{\mathbf{n}} = a\hat{\mathbf{s}} + b\frac{\mathbf{CM''}}{|\mathbf{CM''}|}.$$

The coefficients a and b are determined from the following geometrical relations (Fig. 2b),

$$\hat{\mathbf{n}} \cdot \hat{\mathbf{s}} = -\sin\theta$$

$$\hat{\mathbf{n}} \cdot \frac{\mathbf{CM''}}{|\mathbf{CM''}|} = -\cos i$$

$$\hat{\mathbf{s}} \cdot \frac{\mathbf{CM''}}{|\mathbf{CM''}|} = \sin(i + \theta),$$

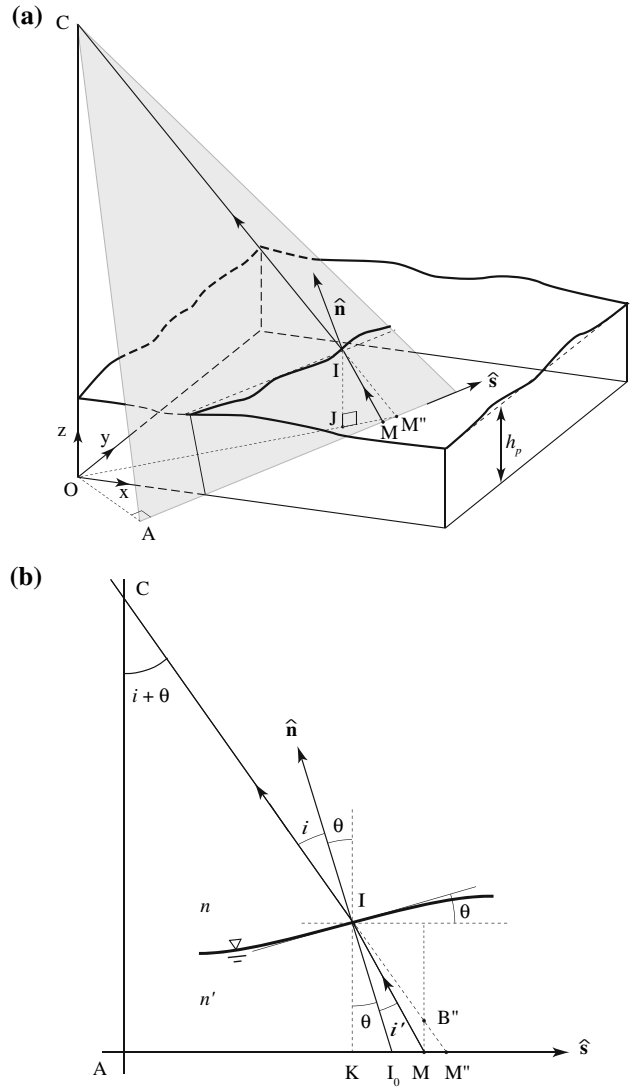

Fig. 2 **a** Three-dimensional ray geometry for an arbitrary deformed interface. The incidence plane CAM is now defined by the object point M, the camera C, and the unit normal vector $\hat{\mathbf{n}}$ at point I where the light ray MIC intercepts the interface. This plane is not vertical in general, and does not contain the optical axis OC. **b** Two-dimensional view of the incidence plane CAM (only the principal ray is shown for clarity). A ray coming from M appears to come from the virtual object B''. In the pattern plane, it appears to come from the point M''

where θ is the angle *measured in the incident plane* between the surface and the horizontal (i.e. the angle of the intersection of the surface with the oblique incidence plane CAM), yielding

$$\hat{\mathbf{n}} = \frac{\sin(i+\theta)\cos i - \sin\theta}{\cos^2(i+\theta)}\hat{\mathbf{s}} + \frac{\sin(i+\theta)\sin\theta - \cos i}{\cos^2(i+\theta)}\frac{\mathbf{CM''}}{|\mathbf{CM''}|}. \quad (6)$$

Within the weak slope and the paraxial approximations, to first order in i and θ, Eq. 6 reduces to

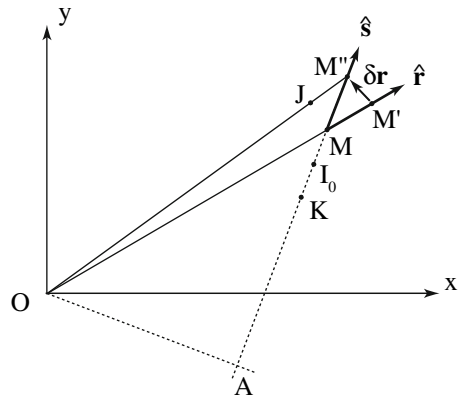

Fig. 3 Top view of the pattern plane, showing the object point M and its two virtual objects M' and M'' for the flat and deformed interface, respectively. The line AMM'' is the intersection of the incident plane CAM with the pattern plane Oxy. J is the vertical projection of the point I where the light ray MIC intercepts the interface. $\mathbf{M'M''} = \delta\mathbf{r}$ is the displacement measured by digital image correlation

$$\hat{\mathbf{n}} = i\hat{\mathbf{s}} - \frac{\mathbf{CM''}}{|\mathbf{CM''}|}. \quad (7)$$

Writing $\mathbf{CM''} = \mathbf{CO} + \mathbf{OM''}$ and taking $|\mathbf{CM''}| \simeq H$, Eqs. 5 and 7 give

$$\nabla h = \frac{\mathbf{OM''}}{H} - i\frac{\mathbf{MM''}}{|\mathbf{MM''}|}. \quad (8)$$

Figure 2b shows that, in the oblique incidence plane CAM, the apparent displacement is given by:

$$\mathbf{MM''} = \mathbf{KM''} - \mathbf{KM} = IK[\tan(\theta+i) - \tan(\theta+i')]\hat{\mathbf{s}}, \quad (9)$$

where K is the projection of I on the line MM''. One has $IK = II_0\cos\theta$, with II_0 along the normal vector $\hat{\mathbf{n}}$, and $II_0 = h(I)/\cos\gamma$, with γ the angle between $\hat{\mathbf{n}}$ and the vertical unit vector $\hat{\mathbf{z}}$ and $IJ = h(I)$ the local height of the interface at the vertical of point I, yielding

$$\mathbf{MM''} = h(I)\frac{\cos\theta}{\cos\gamma}[\tan(\theta+i) - \tan(\theta+i')]\hat{\mathbf{s}}. \quad (10)$$

Considering again small angles, and assuming weak deformations $h(I) \approx h_p$, Eq. 10 becomes:

$$\mathbf{MM''} = \alpha h_p i\hat{\mathbf{s}}, \quad (11)$$

which is similar to Eq. 3, except that now the displacement is along $\hat{\mathbf{s}}$ instead of $\hat{\mathbf{r}}$ (see Fig. 3). Note that the focal surface where lies the virtual object B'' associated to M'' is now deformed according to the shape of the interface (see Fig. 2), so that B'' cannot be exactly focused. However, for weak deformations, this focal surface remains close to the horizontal focal plane at $z = \alpha h_p$ determined for a flat interface (point B' in Fig. 1). In practice, since the characteristic size of the

dots on the pattern is larger than one pixel, this small out of focus effect can be neglected.

From Eq. 11, one has $i\hat{\mathbf{s}} = \mathbf{MM}''/\alpha h_\mathrm{p}$, so that the surface gradient (Eq. 8) becomes:

$$\nabla h = \frac{\mathbf{OM}''}{H} - \frac{\mathbf{MM}''}{\alpha h_\mathrm{p}}. \tag{12}$$

Introducing $\mathbf{OM}'' = \mathbf{OM}' + \delta\mathbf{r}$ and $\mathbf{MM}'' = \mathbf{MM}' + \delta\mathbf{r}$ (with $\delta\mathbf{r} = \mathbf{M}'\mathbf{M}''$) into Eq. 12 yield

$$\nabla h = -\delta\mathbf{r}\left(\frac{1}{\alpha h_\mathrm{p}} - \frac{1}{H}\right) + \frac{\mathbf{OM}'}{H} - \frac{\mathbf{MM}'}{\alpha h_\mathrm{p}}.$$

Finally, recalling Eq. 3, the last two terms cancel (see Fig. 1b), and a simple linear relation between ∇h and $\delta\mathbf{r}$ is obtained,

$$\nabla h = -\frac{\delta\mathbf{r}}{h^*}, \quad \text{with} \quad \frac{1}{h^*} = \frac{1}{\alpha h_\mathrm{p}} - \frac{1}{H} > 0. \tag{13}$$

This demonstrates that, to first order in paraxial angle, surface slope and relative surface deformation, the displacement $\delta\mathbf{r}$ is simply proportional to the surface gradient ∇h. In practice, with a camera far above the imaged surface, $H \gg \alpha h_\mathrm{p}$ (with $\alpha \simeq 0.24$ for an air–water interface), we can simply consider $h^* \simeq \alpha h_\mathrm{p}$.

We recall here that the surface-pattern distance was considered equal to the liquid depth, $h_0 = h_\mathrm{p}$. In practical situations, one or more intermediate materials of various indices are also present between the lower fluid and the pattern, and the distance h_p should be replaced by an effective distance. Consider, for instance, the common situation depicted in Fig. 4, where a glass plate of thickness h_g and an air gap h_a are inserted between the fluid and the pattern. Assuming that the camera is far above the surface, only vertical light rays can be considered, so that the total

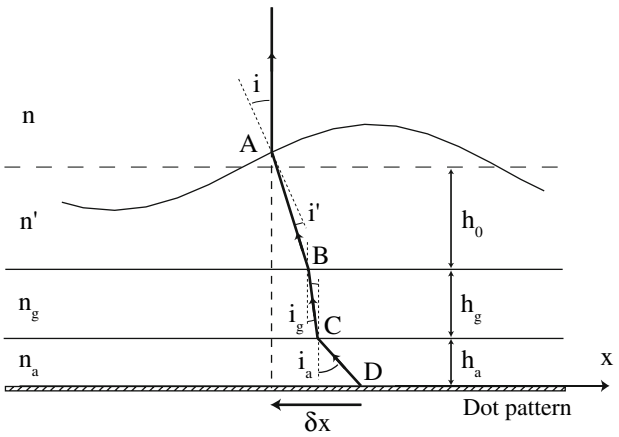

Fig. 4 Apparent displacement δx when several intermediate materials are inserted between the interface and the pattern, assuming that the camera is located far above the surface ($H \gg \alpha h_\mathrm{p}$).In this example, two intermediate layers, denoted g and a (for glass and air) are present, with $n_\mathrm{a} < n' < n_\mathrm{g}$

displacement δx along the direction $\hat{\mathbf{x}}$ is the sum of the elementary displacements, yielding

$$\delta x = \left(-h_0 + \frac{n}{n'}h_0 + \frac{n}{n_\mathrm{g}}h_\mathrm{g} + \frac{n}{n_\mathrm{a}}h_\mathrm{a}\right)\frac{\partial h}{\partial x}.$$

Finally, summing up the displacement components along each direction $\hat{\mathbf{x}}$ and $\hat{\mathbf{y}}$, the result can be written in the form (13), where the effective surface-pattern distance h_p is the sum of the thickness of the layers weighted by the refraction index ratio,

$$h_p = h_0 + \frac{n'}{n_\mathrm{g}}h_\mathrm{g} + \frac{n'}{n_\mathrm{a}}h_\mathrm{a}. \tag{14}$$

Note finally that, considering the finite aperture D (see Fig. 1), the light beam selected by the diaphragm will intercept the interface in a small ellipse of typical size $\delta \approx Dh_\mathrm{p}/H$ around the point I. It is implicitly assumed here that the surface slope is nearly constant within this ellipse, i.e. $\partial^2 h/\partial s^2 \ll \delta^{-1}$. However, this assumption is not critical, since the the curvature $\partial^2 h/\partial s^2$ is also constrained by the much restrictive invertibility condition (see Sect. 2.5) in order to avoid ray crossings.

2.4 Parallax distorsion

If the camera is far above the surface, the points M, M' and M'' are very close, and the displacement $\delta\mathbf{r}$ measured at a point M can be considered as originating from the gradient ∇h at the vertical of M for simplicity. However, the finite camera distance H introduces a parallax distorsion, since the surface gradient is actually measured at the point I (intersection of the light ray MIC with the interface) which is not at the vertical of M.

The location of point J, defined as the vertical projection of I in the horizontal plane (see Figs. 2a and 3), can be expressed by remarking that the two triangles COM'' and IJM'' are similar, so that $JM''/OM'' = IJ/H$. Accordingly, assuming weak deformations (i.e. $IJ = h(I) \simeq h_\mathrm{p}$), one has

$$\mathbf{OJ} = \left(1 - h_\mathrm{p}/H\right)\mathbf{OM}''. \tag{15}$$

If a resolution better than h_p/H is needed for the surface height reconstruction, a remapping of the measured gradient field onto the original reference frame of the pattern, based on a suitable interpolation scheme, has to be performed before the integration. An illustration of this remapping procedure is given in Sect. 4.2.

2.5 Invertibility condition (IC)

In the previous sections, it was implicitly assumed that the displacement field $\delta\mathbf{r}$ could be determined from the refracted image of the pattern. However, this is not true if crossings of light rays occur between the pattern and the

interface, which would result in the formation of caustics, as explained in Fig. 5.

A necessary condition to determine the displacement field $\delta\mathbf{r}$ from the refracted image is that a given image m on the camera should originate from a single object M of the pattern. In the case of a pattern below the interface ($n' > n$), ray crossings may appear below the wave crests, which act as magnifying lenses (Fig. 5). This invertibility condition (IC) requires that the focal length associated to the surface curvature is larger than the surface-pattern distance everywhere in the imaged field. For example, in the case of a sinusoidal plane wave of amplitude η_0 and wavelength λ, $h(x, y) = h_p + \eta_0 \cos(2\pi x/\lambda)$, and approximating the curvature as $\partial^2 h/\partial x^2$, ray crossings are avoided by chosing a surface-pattern distance smaller than the critical distance $h_{p,c}$,

$$h_p < h_{p,c} = \frac{\lambda^2}{4\pi^2 \alpha \eta_0}. \tag{16}$$

Consider, for instance, a wave amplitude of $\eta_0 = 0.5$ mm and wavelength $\lambda = 3$ cm, with $h_p = 3$ cm. The characteristic displacement is given by $|\delta\mathbf{r}| \simeq \alpha 2\pi h_p \eta_0/\lambda \simeq 0.8$ mm (see Eq. 13, assuming $H \gg \alpha h_p$). In this situation, caustics would form well below the surface, at a distance of $h_{p,c} = 18$ cm, so that accurate measurements of the displacement field can be readily achived when taking $h_p = 3$ cm.

The invertibility condition 16 may be more conveniently formulated directly from the displacement field. Consider ℓ' and ℓ'' the abscissa of the virtual objects M' and M'' (for the flat and deformed interfaces respectively) taken along any arbitrary direction $\hat{\boldsymbol{\ell}}$. To avoid ray crossing, ℓ'' has to be a strictly increasing function of ℓ', i.e., $\partial\ell''/\partial\ell' > 0$. Denoting $\delta\ell = \delta\mathbf{r} \cdot \hat{\boldsymbol{\ell}} = \ell'' - \ell'$ the displacement along $\hat{\boldsymbol{\ell}}$, and introducing the strain $\sigma = \partial\delta\ell/\partial\ell'$ along $\hat{\boldsymbol{\ell}}$ (one has $\sigma > 0$ and < 0 for magnified and reduced images respectively), the condition for no ray crossing is $\sigma < 1$. In terms of the magnification factor $m = \partial\ell'/\partial\ell'' = 1/(1-\sigma)$ along $\hat{\boldsymbol{\ell}}$, this condition simply writes $m > 0$.

Satisfying the condition for no ray crossing for arbitrary direction requires that the largest (extensional) strain remains everywhere bounded by 1 (note that there is no limitation in principle for the compressive strain when $n' > n$). Formally, denoting $\sigma_1 < \sigma_2$ the two ordered principal strains (these are the eigenvalues of the strain tensor $\partial\delta r_i/\partial x_j$), the invertibility condition (IC) is

$$\sigma_2 < 1 \tag{17}$$

at each point of the field. For instance, a plane wave produces an oscillating (compressive and extensional) strain along the direction of propagation and zero strain along the perpendicular direction, so that σ_2 shows oscillations clipped at 0.

Criterion 17 is clearly an a posteriori test, since the computation of the principal strains requires the displacement field to be determined, which is possible only if Eq. 17 is satisfied. However, the measurement of the principal strains provides an interesting test of *how far* the light rays are from crossing. An empirical criterion based upon the largest absolute principal strain is discussed in Sect. 5.

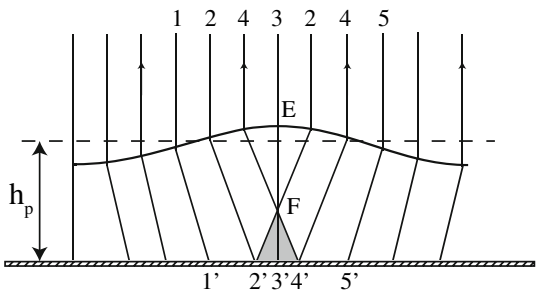

Fig. 5 Large curvature of the interface or large pattern-surface distance induce ray crossings when the invertibility condition (IC) is not satisfied, Eq. 16. Here the pattern-surface distance h_p (taken equal to the liquid depth h_0) is larger than the focal length EF of the point of maximum convex curvature, under the wave crest. The sequence of points $2'3'4'$ on the pattern will be seen as 432, with $2'$ and $4'$ having multiple images

3 Set-up and numerical methods

3.1 Experimental set-up

Experiments were carried out in a 60 cm × 40 cm glass tank, filled with tap water up to an height h_0 of the order of a few centimeters (Fig. 6). The water depth is measured by a depth gauge with a 0.1 mm resolution.

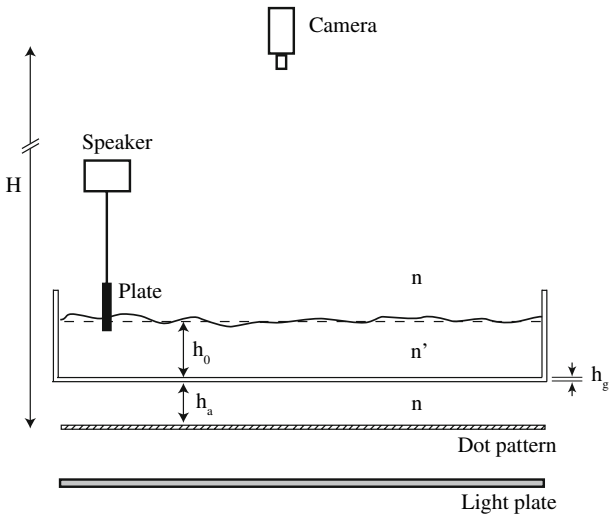

Fig. 6 Sketch of the experimental set-up (camera above, configuration 1). Not at scale, $h_0/H \sim 1{,}000$

Two series of experiments were carried out: Validation experiments, performed with a 2,048 × 2,048 camera at 8 frames per second (Sect. 4), and some time-resolved experiments of drop impacts, with a 1,280 × 1,024 camera at 100 frames per second (Sect. 6). For most experiments, the camera is located above the water tank (configuration 1), at a distance $H = 2.0$ m from the pattern, and the imaged area is a square of side $L = 14$ cm. The maximum paraxial angle is $\beta_{max} = L/(\sqrt{2}H) \simeq 2.8°$. In this case, the pattern is placed below the transparent bottom of the tank, of thickness $h_g = 5$ mm, and an additional air gap of adjustable thickness h_a may also be present between the glass plate and the pattern. For experiments where the camera is located below the water tank (configuration 2), a 45° standard glass-silvered mirror is placed below the tank, and the total camera-pattern distance is $H = 2.9$ m.

The imaged pattern has been carefully designed to allow for unambiguous reconstruction of the displacement field by the DIC algorithm with a good spatial resolution. The camera resolution and the expected displacement magnitude have to be taken into account to optimize the characteristic size of the fine structure of the pattern. In order to maximize the quantity of information and to reduce fortuitous coincidences, a set of randomly distributed dots, partially overlaping, is used. In the example shown in Fig. 7, dots of diameter 0.4 mm, made of concentric circles of increasing grayscale, with an overall black-on-white density ratio of approximately 1:2, have been numerically generated. The pattern is printed on an overhead transparency using a standard 1,200-dpi Laserjet printer, and is lighted using a uniform lighting plate. It must be noted that, due to the halftoning rendering of the printer, the actual resolution of the pattern is significantly lower than the nominal 1,200 dpi, especially when overhead transparencies are used. The resulting dot diameter in Fig. 7, as imaged by the $2{,}048^2$ camera, is approximately 6 pixels.

3.2 Displacement field computation

A reference image of the pattern is taken when the air/water interface is flat, and a second image or a movie is taken during the experiment. The displacement field $\boldsymbol{\delta r}$ between each image and the reference image is obtained by the DIC algorithm available in the commercial software DaVis.

Interrogation windows of size 16 × 16 pixels, with an overlap of 8 pixels, are used for the computations of the correlation functions. Although the dot diameter of 6 pixels is larger than the optimal size of 2–3 pixels usually recommended for PIV applications (Raffel et al. 1998), the high "seeding" density used here allows to satisfy the criterion of approximately 5 dots per interrogation window (see Fig. 7). The final displacement field is defined on a 256 × 256 grid, with a spatial resolution of order 0.5 mm (the numbers given here correspond to the 2,048 × 2,048 camera). Classical postprocessing schemes are applied, such as median filter to remove bad vectors. An example of displacement field obtained for plane waves is shown in Fig. 8.

The uncertainty of the cross-correlation method is already well documented, e.g., in the literature for PIV (Raffel et al. 1998). Since the random dot pattern is generated to meet the requirements for an optimal cross-correlation resolution, one may expect to reach the theoretical resolution of this method. Using interrogation windows of decreasing size, with final size of 16 × 16 pixels, a resolution of 0.1 pixel (about 7 μm) can be achieved using a classical subpixel interpolation scheme for the maximum of the correlation function. For typical

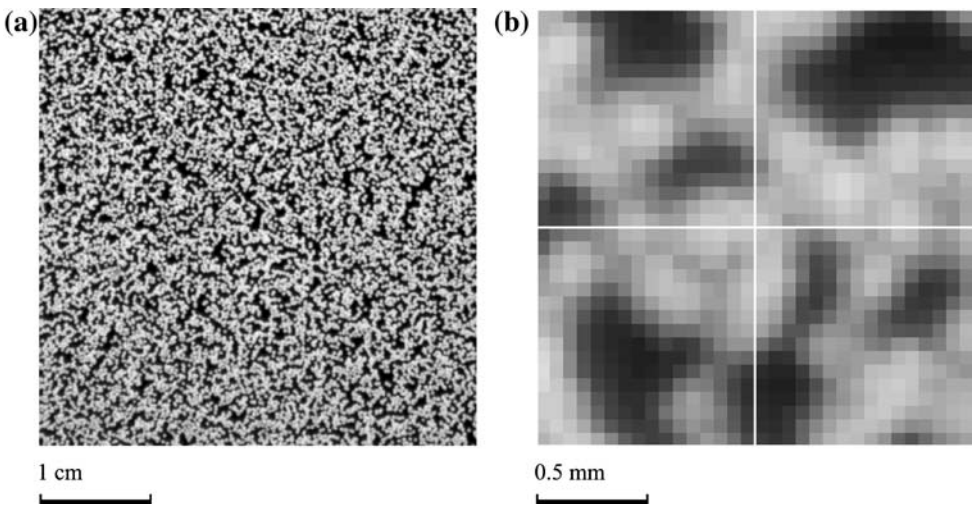

Fig. 7 Magnifications at scales 1:1 (**a**) and 20:1 (**b**) of the random dot pattern used in the present experiments, as imaged by the $2{,}048^2$ pixels camera on a 14 × 14 cm field. Dots of diameter $d = 0.4$ mm were numerically generated, with a density of 50%, resulting in dots of approximately 6 pixels in the camera sensor. The magnification (**b**) represents 32 × 32 pixels, and four interrogation windows of size 16 × 16 pixels, used for the digital image correlation, are shown for reference

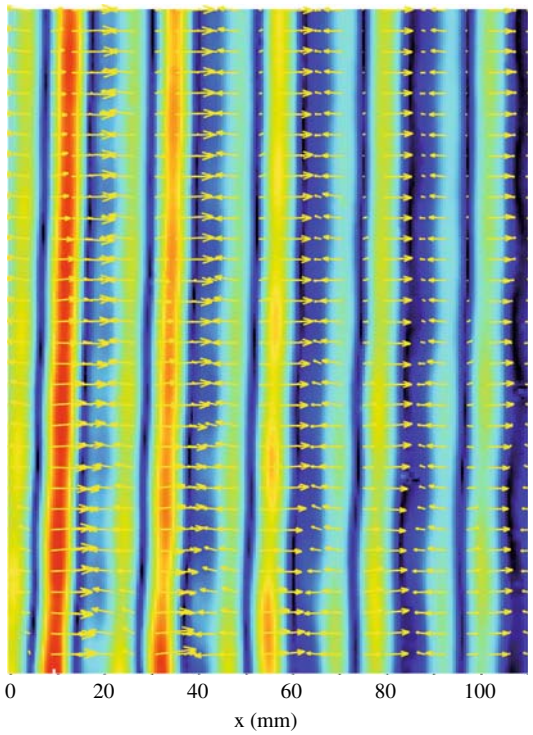

Fig. 8 Displacement field for an approximately plane wave, generated from a vibrated plate on the left. Color codes the displacement norm

displacement of order 5 pixels, and assuming moderate strain so that the dots remain essentially circular, this relative uncertainty is about $\epsilon = 2 \times 10^{-2}$. Larger values may however be expected when the refracted pattern is significantly strained. Note also that decreasing the window size would result in a better spatial resolution, but worse displacement resolution.

3.3 Surface height reconstruction

The numerical integration of the surface height field $h(x, y)$ from the displacement field $\boldsymbol{\delta}\mathbf{r}(x, y)$ requires the computation of the inverse gradient operator, ∇^{-1}. Denoting $\boldsymbol{\xi} = -\delta\mathbf{r}/h^*$ the measured surface gradient, see Eq. 13, we have to compute

$$h(x, y) = h_{\mathrm{p}} + \nabla^{-1}\boldsymbol{\xi}. \tag{18}$$

This integration is performed by a numerical inversion of the linear system built from the second-order centered difference gradient operator. Since the gradient field $\boldsymbol{\xi} = \xi_x\hat{\mathbf{x}} + \xi_y\hat{\mathbf{y}}$ is defined on a $M \times N$ grid, this linear system has 2 MN equations and MN unknown. A solution may however be defined for this over-determined linear system: the resulting surface height $h(x, y)$ is the "best" solution in the least-square sense, i.e., the solution minimizing the residual $||\nabla h - \boldsymbol{\xi}||^2$. An example is shown in Fig. 9 for an approximately plan wave. The details of the numerical integration method are discussed in the Appendix 1.

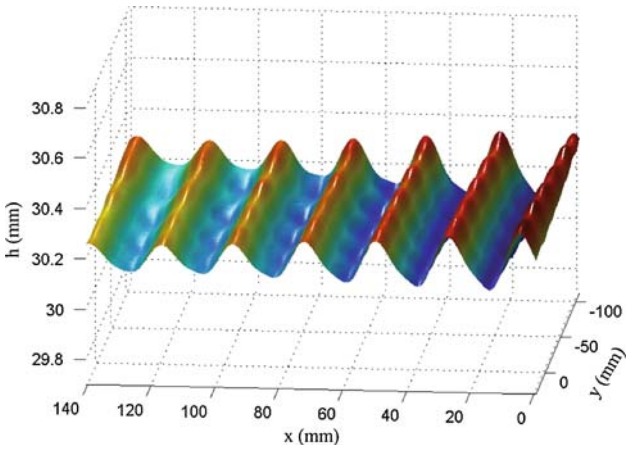

Fig. 9 Perspective view of the reconstructed surface height of an approximately plane wave, propagating from right to left, showing a slight transverse modulation

An alternative method for the inversion of the gradient operator using Fourier transform has been proposed by Zhang et al., but suffered from border effects and was limited to rectangular domains (Zhang and Cox 1994; Zhang et al. 1996; Zhang 1996). The least-square inversion method proposed here is similar to the one introduced in Roesgen et al. (1998), which was based on the hexagonal lattice implied by the specific geometry of their microlens array. Here the inversion is expressed in a simpler Cartesian lattice, which is easier to implement and suitable for the processing of the surface gradient data obtained from typical DIC algorithms.

Note that the displacement field $\delta\mathbf{r}$ being irrotational in principle, this property may be used as a constrain to improve the measurement of the maximum of the correlation function. However, if a residual rotational component is present in the displacement field $\delta\mathbf{r}$, it will not contribute to the integrated surface height, and a classical unconstrained DIC algorithm has been used here.

Being non-local, the least-square solution $h(x, y)$ is robust to localized bad vectors. This method is suitable for square or rectangular areas, but may be delicate to implement for more complex geometries (see Appendix 1). A strong limitation of this method is its inability to detect changes of the mean surface height, originating for example from waves of characteristic length of the order or larger than the imaged area. Another example is provided by a wavepacket entering into the imaged area, producing an artificial change of the mean height of the unperturbed surface.

It is worth noting that some vibrations in the optical setup may have a strong influence on the reconstructed surface height. In our experiments, vibrations in the camera position due to the internal cooling fan were found to

produce an apparent circular translation of the image of about 5 μm (about 0.1 pixel) when imaging at a distance of 2 m. Although very weak, the resulting uniform displacement field, once integrated, produces a noticeable mean slope which superimposes to the measured height field. This uniform displacement can be readily substacted before integration, but prevents from the measurement of slopes of characteristic length of the order or larger than the imaged area.

3.4 Resolution

The integration method for solving Eq. 18 being linear, the relative uncertainty of the surface height reconstruction is expected to depend linearly upon the uncertainty ϵ of the input displacement field. Based on numerical tests (described in the Appendix 2), assuming a displacement field perturbed with an additive, spatially uncorrelated, Gaussian noise of relative magnitude ϵ, the resolution of the surface reconstruction is found to be

$$\frac{\Delta\eta}{\eta_{\mathrm{rms}}} \simeq 5\frac{L}{\lambda}\frac{\epsilon}{N}, \tag{19}$$

Taking $L = 14$ cm, $\lambda = 3$ cm, $N = 256$ and $\epsilon = 0.02$ gives $\Delta\eta \simeq 10^{-3}\eta_{\mathrm{rms}}$: a wave of amplitude 1 mm should be measurable with a precision of 1 μm.

However, the estimate given by Eq. 19 should be considered as a lower bound for the true uncertainty. First, the displacement field noise ϵ may be larger than 2% when large strains are present. Moreover, a noise with significant spatial correlation is likely to be produced by the DIC algorithm: patterns with fortuitous coincidence, or optical defects (impureties, reflections) result in clustered bad vectors, and strongly strained refracted patterns will produce bad vectors correlated with regions where displacements or displacement variations are large.

4 Validation experiments

4.1 Validation of the slope measurement

A first validation experiment has been carried out to assess the accuracy of the displacement field measurement, using the deflection of a reflected laser beam. Plane waves were generated by oscillating a PVC plate attached to a speaker. The plate length is equal to the tank width, and generates nearly plane waves. A laser beam, making an angle of $\phi = 17°$ with the horizontal, is reflected at a given point of the surface, and the reflected beam is visualized on a vertical screen located 1 m from the reflection point (Fig. 10). An angle of θ of the liquid surface results in an angle of $\phi + 2\theta$ of the reflected

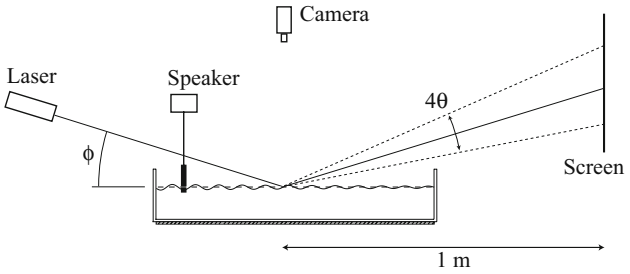

Fig. 10 Setup for the validation of the slope measurement. The laser beam deflection angle is twice the surface local slope

beam. Plane waves have been generated with various amplitudes, at a fixed frequency of 10 Hz. For each amplitude, the peak-to-peak deviation of the reflected beam is measured on the screen, and the displacement field measured by synthetic Schlieren in a small area around the reflecting point is determined independently.

The maximum slopes $\xi = \tan\theta$ measured from the two methods are compared in Fig. 11. The error bars result from the non-strictly sinusoidal wave produced by the wavemaker, producing higher frequency oscillations of the reflected beam around the main oscillation. Although the uncertainty of each data point is significant, a nearly perfect correlation between the two methods is obtained. The measurements have been restricted to $\xi < 0.1$, for which non-harmonic effects can be neglected. Larger slopes are obviously measurable for the correlation algorithm, but they could not be compared to the ones measured from the beam deflection method because of the uncertainties due to the higher order modes.

4.2 Validation of the surface height reconstruction

In order to test the full measurement procedure (slope measurement, surface reconstruction and parallax distorsion),

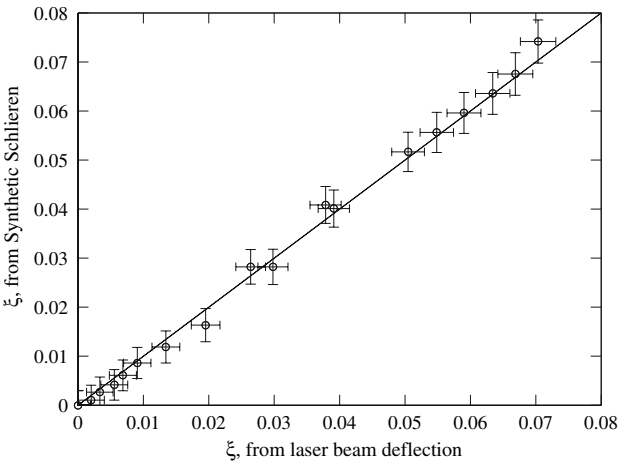

Fig. 11 Comparison of the maximum slopes measured independently by the laser beam method and by synthetic Schlieren

a solid model of a wavy surface with a well controlled geometry has been used. A sinusoidal plane wave of wavelength 20 mm and amplitude 0.5 mm was carved on the upper surface of a 23 mm thick parallelepiped plexyglass plate of size 10 × 14 cm by a computer controlled milling machine with a 1 mm diameter hemispherical tool. A similar plexyglass plate with a flat upper surface was used for the reference image.

Figure 12 shows the reconstructed profile of the plexiglass model as a function of x along the line $y = 0$. In order to quantify the influence of the parallax, the plexiglass model was placed at a location $x = 20$–120 mm off the optical center, and the camera was located at a moderate distance of $H = 1.55$ m from the dot pattern. The wavelength measured from the raw profile (without the remapping correction) is 20.30 ± 0.05 mm, which over-estimates the expected value of about 1.5%. After application of the remapping correction Eq. 15, the measured wavelength and amplitude are 20.01 ± 0.05 mm and 1.03 ± 0.02 mm, in remarkable agreement with the expected values.

5 Influence of the pattern-surface distance

An important feature of the FS-SS method is the maximum acceptable strain for a reliable reconstruction of the surface height. For a given free surface topography, the strain of the refracted image is essentially controlled by the surface-pattern distance h_p. This parameter should be set as large as possible to increase the resolution, but smaller than the critical distance (Eq. 16) where ray crossings appear.

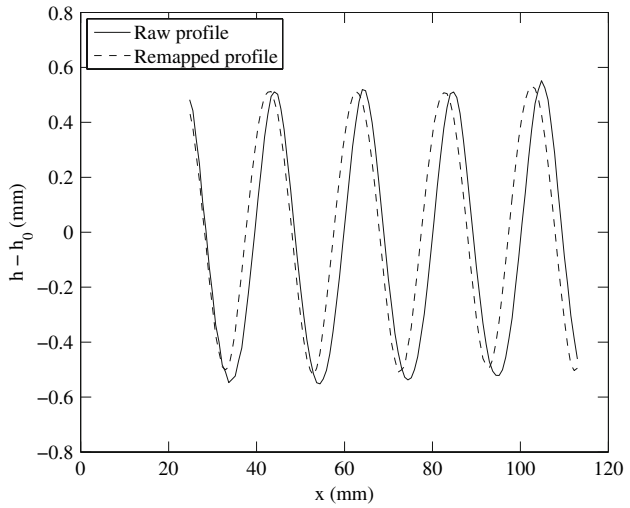

Fig. 12 Surface profile measured on a plexiglass model machined with a sinusoidal plane wave of wavelength 20 mm and amplitude 0.5 mm. The opical axis is located at $x = 0$ mm, and the model is placed off-axis *continuous line* represents raw profile, *dotted line* represents remapped profile using Eq. 15, correcting for the parallax distorsion.

However, even for $h_p < h_{p,c}$, although no ray crossing is present, regions of large strain (either compression or extension) may prevent from an accurate measurement of the displacement field, and a looser criterion than Eq. 17 is desirable to assess the measurement accuracy.

A systematic series of experiments has been carried out, varying the air gap between the bottom glass plate and the pattern, h_a, in the range 0–300 mm, so that the pattern-surface distance h_p (corrected by the intermediate air and glass layers, see Eq. 14) is varied between 30 and 430 mm. Plane waves, of amplitude 0.15 mm and wavelength 22 mm, are generated in a 22-mm depth water layer. For each value of h_a a reference image with flat interface and a series of images with the waves are taken.

Five examples are shown in Fig. 13. Only a 2 × 2 cm square is shown, whose location is chosen to show similar wave pattern for each h_p. As h_p is increased, the refracted image of the pattern above the wave crests show increasingly elongated patches. In this situation, the cross-correlation algorithm is likely to produce wrong results, since the location of an initial circular patch of the reference image may be matched all along the ellipse of the refracted image.

Since in most situations curvatures of both sign are equally present, a convenient indicator which gets rid of the ordering of the principal strains is provided by the largest absolute principal strain field,

$$\sigma^*(x,y) = \max(|\sigma_1(x,y)|, |\sigma_2(x,y)|)$$

Large values of σ^* indicate both regions of strong compression (under troughs) or strong extension (under crests). Since the integration method is non-local, one has to check that the largest value of σ^* over the whole field remains moderate. However, some bad vectors from the cross-correlation may produce non-physical large σ^*, preventing from using a simple criterion based on $\max_{x,y} \sigma^*$. It was found that, in a roughly homogeneous region, a quite robust criterion may be built from the root-mean-square of this quantity,

$$\sigma^*_{\mathrm{rms}} = \sqrt{\frac{1}{N_x N_y} \sum_{x,y} \sigma^{*2}(x,y)}.$$

Reliable results were obtained when the rms principal strain satisfies

$$\sigma^*_{\mathrm{rms}} < 0.15. \qquad (20)$$

This criterion corresponds here to an air gap of $h_a = 50$ mm (see picture 4 in Fig. 13), which shows a maximum strain of 0.71 (magnification factor $m = 1/(1 - \sigma) \simeq 3.5$ under the wave crests). Figure 14, where cuts of the surface height along the x direction are shown for the different values of h_a, confirms that no change are detectable for h_a up to 50 mm. This criterion gives the maximal screen-pattern distance for a reliable measurement of a given

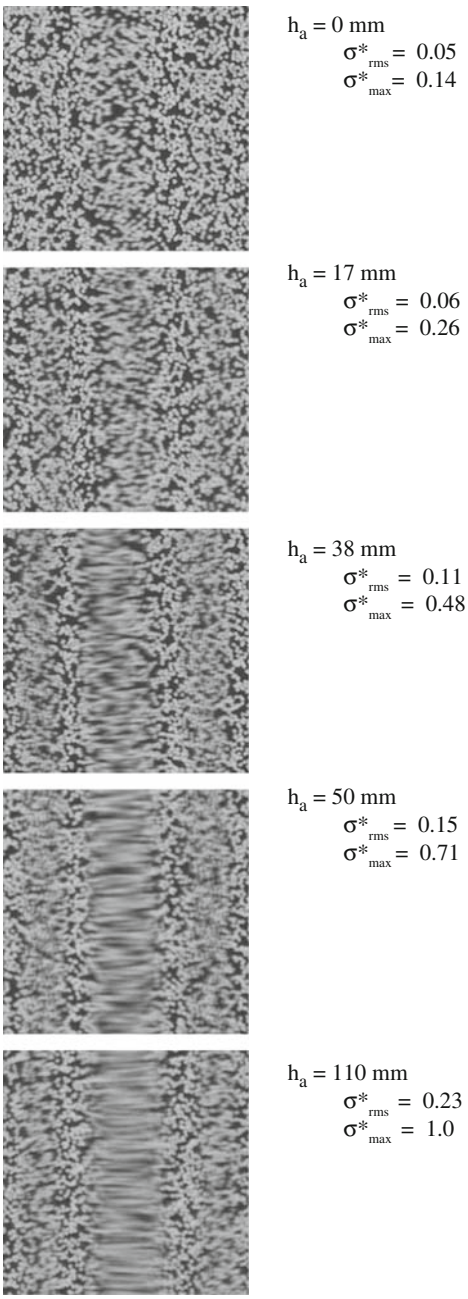

Fig. 13 Snapshots of the refracted image for five values of the air gap h_a between the glass plate and the pattern. Only a 2 × 2 cm square is shown (the whole field is 14 cm). Blurry elongated horizontal segments appear under the wave crests at large h_a

surface curvature or, equivalently, the largest curvature measurable for a given distance. In practice, a safe choice would be $\sigma^*_{\rm rms} \simeq 0.05-0.10$.

6 Circular wave generated by a water drop impact

Time-resolved visualizations of the circular wave pattern generated by the impact of a water drop have been finally

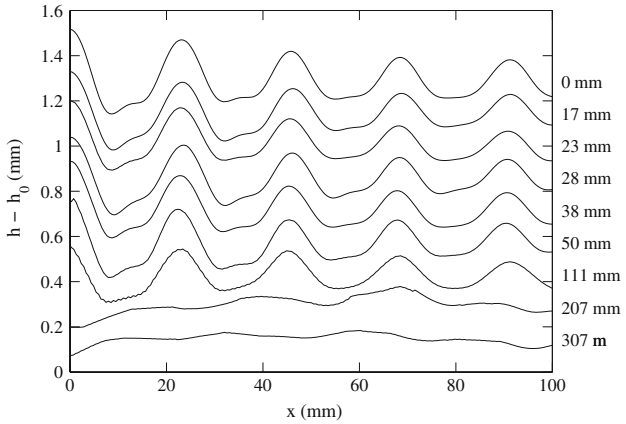

Fig. 14 Surface height of the same waves, measured with different air gap h_a between the pattern and the glass bottom of the tank. The profiles are shifted vertically

carried out, aiming to demonstrate the ability of the FS-SS method to investigate complex wave phenomena. A water drop of 1 mm diameter is dropped one centimeter above a 4 cm water layer at time $t = 0$, and the surface height is reconstructed on a 20 × 20 cm^2 field at 100 Hz. The invertibility condition was satisfied only 0.4 s after the impact.

The two perspective views of the surface elevation in Fig. 15 clearly shows the growing circular wavepacket. The largest waves have amplitude of 100 μm and wavelength of order of 30 mm, but much smaller waves, of amplitude of 1 μm and wavelength around 10 mm, can also be distinguished at the front of the wavepacket. Shortly after the impact, the surface near the impact is almost perfectly flat, showing only residual plane waves of amplitude less than 1 μm originating from slight background vibrations from the lateral tank walls.

Phase and group velocities may be estimated from the spatio-temporal diagrams shown in Fig. 16. In these diagrams the surface elevation along a radial line is represented in color scale as a function of time. The phase velocities (measured here as the slope following a given wave crest) are 26 cm/s near the rear, for the largest wavelengths, and 23 cm/s near the front, for the smallest ones. The front velocity is found to be close to the expected minimum phase velocity for capillary-gravity waves in deep water, $c_{\rm min} = (4\gamma g/\rho)^{1/4} \simeq 23.1$ cm/s for $\lambda_c = 2\pi(\gamma/\rho g)^{1/2} \simeq 17$ mm (here $\gamma \simeq 0.070$ N/m is the air–water surface tension, ρ the water density and g the gravity). The measured rear velocity of the wavepacket is 18 cm/s, a value which compares well to the expected minimum group velocity, $c_{g,\rm min} \simeq 17.7$ cm/s. Since the phase velocity is larger than the front velocity at the rear edge, new wave crests appear at the rear and travel along the wavepacket. On the other hand, the front edge

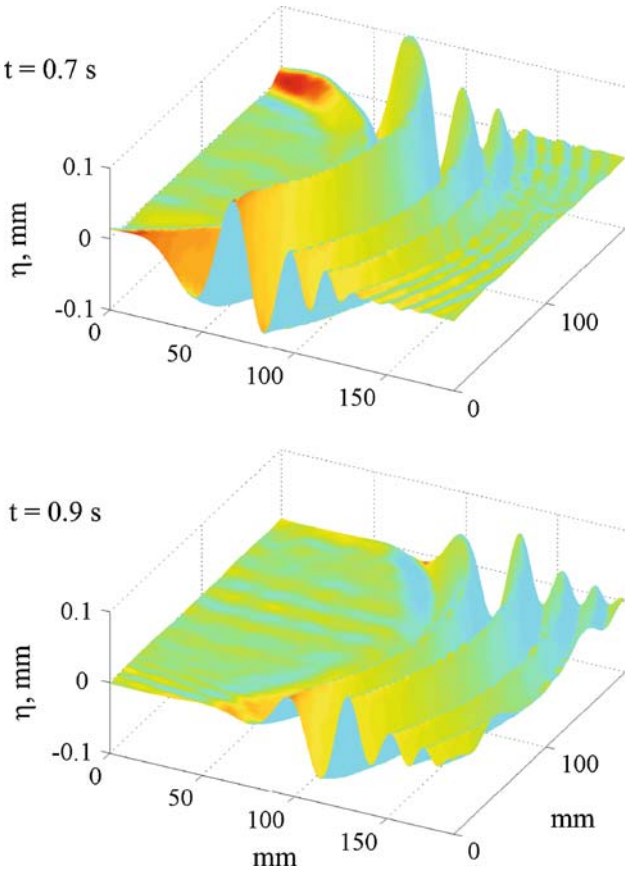

Fig. 15 Perspective view of the circular waves created by the impact of a drop, at times $t = 0.7$ and $t = 0.9$ s after the impact

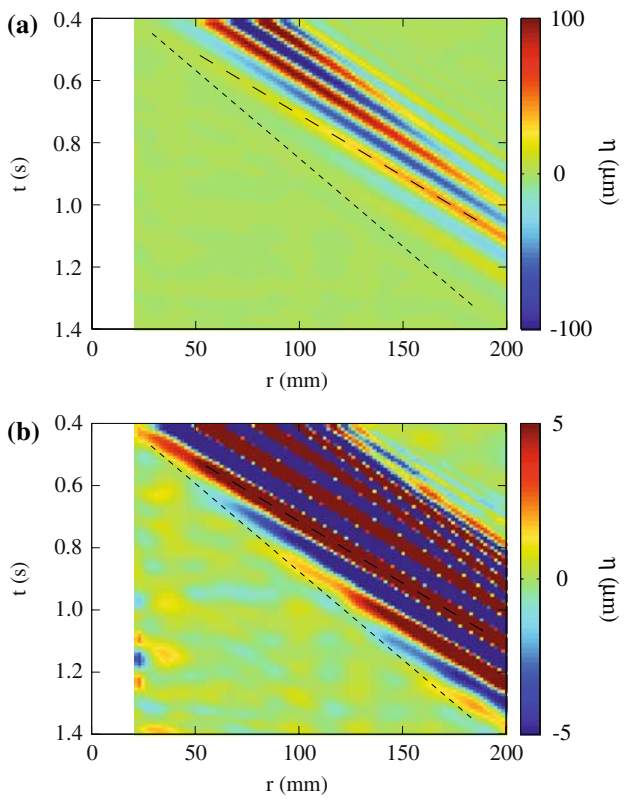

Fig. 16 Spatio-temporal diagram of the surface height profile taken along a radius of the circular wave shown in Fig. 15. Only the color scale is changed between (**a**) and (**b**). The *long dashed line* shows the phase velocity of a wave crest, and the *short dashed line* shows the rear front velocity of the wavepacket (approximate group velocity)

velocity can be hardly determined from those diagrams, because of capillary waves of very weak amplitude which have their wavecrest line almost parallel to the wavepacket border itself.

7 Conclusion

The FS-SS method presented in this paper relies on the same ground as the synthetic Schlieren (or equivalently Background-oriented Schlieren) method, namely the quantitative analysis of the refracted image of a random dot pattern when viewed through a deformed interface, following the works of Kurata et al. (1990) and Elwell (2004).

To first order in paraxial angle, surface slope and the relative surface deformation, we have shown that the displacement field is simply proportional to the surface gradient (Eq. 13). Compared to the classical synthetic Schlieren method, which is applied in situations where the refraction index varies continuously, here the step-like variation of the index at the interface allows for a complete reconstruction of the topography of the interface from the measured surface gradient. This low-cost and versatile optical method gives quantitative measurement with a vertical resolution of order of 2% of the maximum deformation amplitude. The numerical reconstruction of the surface height, being based on a least square inversion of the gradient operator, is very robust and has a low computational cost. When used with a high speed imaging system, this method allows for time-resolved investigation of complex wave phenomena.

The main limitations of the FS-SS method are:

1. Being based on the measurement of the surface gradient, it is not able to detect uniform changes of the surface height.
2. It is extremely sensitive to slight vibrations (including vibrations generated by the internal fan of a cooled camera).
3. It is unable to determine the displacement field for strong curvature and/or large surface-pattern distance.
4. It applies only for weak deformations, weak slopes and weak paraxial angle.

Limitation no. 2 can be circumvented by substracting the mean displacement field before numerical integration.

However, this substraction prevents from measuring mean surface slopes of characteristic scale of the order or larger than the imaged area. Applications where the measurement of a constant slope is needed would require an extremely stable optical setup.

For the limitation no. 3, an empirical criterion has been proposed, based on the rms strain, namely $\sigma^*_{\mathrm{rms}} < 0.15$, Eq. 20, where σ^* is the largest absolute principal strain. Note however that this constrain is partly due to the use of a DIC algorithm for the measurement of the displacement field, which produces wrong results for strongly strained images. Other approaches, such as the Optical Flow (Barron et al. 1994), may behave better than DIC in this situation, and may allow to work closer to the theoretical invertibility condition (IC) given by $\sigma_2 = 1$, where σ_2 is the largest principal strain.

Finally, the limitation no. 4 is probably the most restrictive for this method. Best accuracy can be actually achieved by maximizing the distance H between the camera and the pattern, so that nearly vertical refracted rays enter the camera. However, even for vanishing paraxial angles, a fully consistent formulation of the problem beyond a first-order approximation with respect to the surface slope and relative amplitude is a very delicate task, which is left for future investigation.

A possible application of FS-SS is the measurement of the contact angle and the dynamics of the wetting of a drop on a substrate (Moisy et al. 2008). Although a slope discontinuity is present at the contact line, the surface curvature along a radius (second derivative) is large but positive, so no ray crossing occurs and the method should apply. However, in order to minimize the relative surface-pattern height changes, a gap between the (transparent) substrate and the pattern should be used.

Finally, wave turbulence is another application where FS-SS may be useful. Here the major limitation is certainly the formation of caustics under the largest curvature at small scales, even if the configuration 2 (camera below and pattern above the surface) is chosen. If applicable, this method should be able to provide the true spatial spectrum of the wave fields, instead of the temporal spectrum usually obtained from classical one-point measurements.

Acknowledgments The authors whish to thank Harold Auradou, Raphael Pidoux, Edouard Pinsolle, Joran Rolland and Jacopo Seiwert for their help during the experiments, Maurice Rossi for enlightening comments on the optical part, and the Reviewers for pointing key references. Guy Demoment and John D'Errico are also acknowledged for fruitful discussions about the algorithm of inversion of the gradient operator, and Francois Lusseyran and Luc Pastur for interesting discussions about the use of Optical Flow algorithms. This work was supported by the ANR grant no. 06-BLAN-0363-01 "HiSpeedPIV".

Appendix 1: Numerical integration of the inverse gradient operator

We seek the solution $h(x, y)$ given the two local slope components ξ_x and ξ_y measured at each point. We first note that a naive integration along one single arbitrary path joining a reference point (0, 0) and a given point (x, y), e.g.

$$\eta(x,y) = \eta(0,0) + \int_0^x \xi_x(x',0)\mathrm{d}x' + \int_0^y \xi_y(x,y')\mathrm{d}y',$$

would suffer from an important noise accumulation effect: a wrong measurement of the slope ξ_x or ξ_y at a given point would propagate along the whole path. Consider, for instance, a one-dimensional signal $\eta(x)$, from which a perturbed local slope $\tilde{\xi} = \partial\eta/\partial x + \epsilon\xi_{\mathrm{rms}}a$ is measured on a discrete set of points, with a is a Gaussian noise of zero mean and unit variance. Computing the perturbed signal $\tilde{\eta}(x)$ from a cumulative sum introduces a drift, as $(\tilde{\eta} - \eta)_{\mathrm{rms}} = \epsilon\xi_{\mathrm{rms}}\sqrt{n}$, where n is the number of grid steps.

For the 2D problem, this drift problem may be partially overcome by averaging over all possible paths joining the reference point (0, 0) to any desired point (x, y). Summing ξ_x from 0 to x averaged over each horizontal stripe for each y, and vice-versa for ξ_y, would lead to a relative uncertainty for η equals to that for $\boldsymbol{\xi}$.

A more efficient and accurate approach consists in writing the gradient operator using linear algebra. Noting H the vector of length MN representing the height field $h(x, y)$ sampled on a $M \times N$ grid, the two vectors of length MN representing each component of the gradient field can be written

$$\begin{aligned} \mathsf{G}_x\mathsf{H} &= \Xi_x, \\ \mathsf{G}_y\mathsf{H} &= \Xi_y \end{aligned} \tag{21}$$

where G_x and G_y are two sparse matrices, of size $MN \times MN$, defining the linear combinations of the elements of H to produce each gradient. G_x and G_y may be defined to produce second-order centered differences, with suitable treatment of the border elements. These two systems (21) may be merged into a single linear system,

$$\mathsf{G}\mathsf{H} = \Xi, \tag{22}$$

where now $\mathsf{G} = (\mathsf{G}_x, \mathsf{G}_y)^{\mathrm{T}}$ is a rectangular sparse matrix of size $2MN \times MN$, and $\Xi = (\Xi_x, \Xi_y)^{\mathrm{T}}$ is a vector of length $2MN$. This system thus gives $2MN$ equations with MN unknowns. It is over-determined, so a direct inversion is not possible. However, an estimate of H may be obtained, by minimizing the residual

$$||\mathsf{G}\mathsf{H} - \Xi||^2 \tag{23}$$

This method produces a solution of the over-determined linear system (22) in a least squares sense. Using Matlab, a convenient and efficient implementation of this algorithm of least-square solution for over-determined linear systems is available with the "\" (backslash) operator. A complete solution based on Matlab for inverting a 2D gradient using second-order centered differences is available using `intgrad2` (D'Errico, http://www.mathworks.com/matlabcentral/).

Although this approach is most easily implemented for rectangular domains, more complex geometries can also be considered. For domains of arbitrary shapes, a rectangular $2Q \times Q$ (where Q is the number of points of the domain) matrix$\mathsf{G}$, whose elements produce the finite differences over each point of the domain, has to be constructed. From this matrix$\mathsf{G}$, the estimate for H is obtained by minimizing Eq. 23 as before.

Appendix 2: Resolution of the numerical integration

From the measurement of local slope $\boldsymbol{\xi}$ at each grid point, with a relative uncertainty given by that of the displacement ϵ, we estimate here the uncertainty $\Delta\eta$ arising from the numerical integration of Eq. 18.

An empirical estimate for $\Delta\eta$ has been obtained from a series of numerical tests. A sinusoidal wave $\eta(x, y)$, of wavelength $\lambda = 2\,\pi/|\mathbf{k}|$ and amplitude η_0, is considered in a square domain of size $[0, L]^2$ discretized to N^2 collocation points. The discrete gradient $\boldsymbol{\xi}$ is computed from a second order finite different scheme, and a Gaussian noise $\mathbf{a}$ is added,

$$\tilde{\boldsymbol{\xi}} = \boldsymbol{\xi} + \epsilon\xi_{\mathrm{rms}}\mathbf{a},$$

where a_x and a_y are of zero mean and unit variance. We further assume that $\mathbf{a}$ and $\boldsymbol{\xi}$ are uncorrelated, and that $\mathbf{a}$ has no spatial correlation. Computing the surface height $\tilde{\eta}$ from the numerical integration of the perturbed gradient $\tilde{\boldsymbol{\xi}}$ yields $\tilde{\eta} = \eta + \epsilon\xi_{\mathrm{rms}}\nabla^{-1}\mathbf{a}$. From this, the rms of the difference height is computed, $\Delta\eta_{\mathrm{rms}} = (\tilde{\eta} - \eta)_{\mathrm{rms}} = \epsilon\xi_{\mathrm{rms}}(\nabla^{-1}\mathbf{a})_{\mathrm{rms}}$.

The following parameters have been systematically varied: the relative noise ϵ from 1 to 8%, the number of points N from 32 to 256, the wavelength λ from 0.1 L to L and the amplitude η_0 from 0.01 L to 0.1 L. For each set of parameters, the results are averaged from 10 realizations with random orientation of the wavevector $\mathbf{k}$. The following empirical law is obtained,

$$\frac{\Delta\eta}{\eta_{\mathrm{rms}}} = (5.0 \pm 0.2)\frac{L}{\lambda}\frac{\epsilon}{N},$$

where $\eta_{\mathrm{rms}} = \eta_0/\sqrt{2}$ is taken for a sinusoidal wave.

References

Adrian RJ (1991) Particle-image techniques for experimental fluid mechanics. Annu Rev Fluid Mech 23:261–304

Andrieu C, Chatenay D, Sykes C (1995) Measuring dynamic contact angles. C R Acad Sci Paris 320:351–357

Barron JL, Fleet DJ, Beauchemin SS (1994) Performance of optical flow techniques. Int J Comput Vis 12(1):43–77

Cox CS (1958) Measurement of slopes of high frequency wind waves. J Mar Res 16: 199–225

Dabiri D, Gharib M (2001) Simultaneous free-surface deformation and near-surface velocity measurements. Exp Fluids 30:381

Dalziel SB, Hughes GO, Sutherland BR (2000) Whole-field density measurements by "synthetic Schlieren". Exp Fluids 28:322–335

DaVis, by LaVision GmbH, Anna-Vandenhoeck-Ring 19, 37081 Goettingen, Germany, complemented with the PIVMat toolbox for Matlab. http://www.fast.u-psud.fr/pivmat

D'Errico J, "Inverse (integrated) gradient" for Matlab. http://www.mathworks.com/matlabcentral/. File 9734

Elwell FC (2004) Flushing of embayments. PhD thesis, University of Cambridge

Hild F, Roux S (2006) Digital image correlation: from displacement measurement to identification of elastic properties—a review. Strain 42:69–80

Jähne B, Riemer KS (1990) Two-dimensional wave number spectra of small-scale water surface waves. J Geophys Res 95:11531–11546

Jähne B, Schmidt M, Rocholz R (2005) Combined optical slope/height measurements of short wind waves: principle and calibration. Meas Sci Technol 16:1937–1944

Keller WC, Gotwols BL (1983) Two-dimensional optical measurement of wave slope. Appl Opt 22:3476–3478

Kurata J, Grattan KTV, Uchiyama H, Tanaka T (1990) Water surface mesurement in a shallow channel using the transmitted image of a grating. Rev Sci Instrum 61(2):736

Lange PA, Jähne B, Tschiersch J, Ilmberger I (1982) Comparison between an amplitude-measuring wire and a slope-measuring laser water wave gauge. Rev Sci Instrum 53:651

Liu J, Paul JD, Gollub JP (1993) Measurements of the primary instabilities of film flows. J Fluid Mech 250:69–101

Meier GEA (2002) Computerized background-oriented Schlieren. Exp Fluids 33:181

Moisy F, Rabaud M, Pinsolle E (2008) Measurement by digital image correlation of the topography of a liquid interface, ISFV13—13th international symposium on flow visualization, and FLUVISU12—12th French congress on visualization in fluid mechanics, paper 326, 1–4 July 2008, Nice

Périe JN, Calloch S, Cluzel C, Hild F (2002) Analysis of a multiaxial test on a C/C composite by using digital image correlation and a damage model. Exp Mech 42:318–328

Raffel M, Willert CE, Kompenhans J (1998) Particle image velocimetry: a practical guide. Springer, Heidelberg

Roesgen T, Lang A, Gharib M (1998) Fluid surface imaging using microlens arrays. Exp Fluids 25:126

Savalsberg R, Holten A, van de Water W (2006) Measurement of the gradient field of a turbulent free surface. Exp Fluids 41:629–640

Sutherland BR, Dalziel SB, Hughes GO, Linden PF (1999) Visualization and measurement of internal waves by 'synthetic Schlieren'. Part 1. Vertically oscillating cylinder. J Fluid Mech 390: 93–126

Tober G, Anderson RC, Shemdin OH (1973) Laser instrument for detecting water ripple slopes. Appl Opt 12(4):788–794

Zhang X (1996) An algorithm for calculating water surface elevations from surface gradient image data. Exp Fluids 21:43–48

Zhang X, Cox CS (1994) Measuring the two-dimensional structure of a wavy water surface optically: a surface gradient detector. Exp Fluids 17:225–237

Zhang X, Dabiri D, Gharib M (1996) Optical mapping of fluid density interfaces: concepts and implementations. Rev Sci Instrum 67(5):1858–1868